CrossMark

The Effect of Temperature on the Formation of Oxide Scales Regarding Commercial Superheater Steels

J. Lehmusto[1] · D. Lindberg[1] · P. Yrjas[1] · L. Hupa[1]

Abstract This study addresses the surface changes of three commercial steels (a low alloy ferritic 10CrMo9-10 steel, a Nb-stabilized austenitic AISI347 steel, and a high alloy austenitic Sanicro 28 steel) by comparing the oxide scale thicknesses, chemical compositions, and surface morphologies of samples after pre-oxidation at 200, 500 and 700 °C with different exposure times (5 and 24 h) under humid or dry conditions. With all three steels, the oxide scale thickness increased as functions of temperature and exposure time, the effect of temperature being more prominent than the effect of exposure time. The presence of water resulted in thicker oxide scales at the studied low alloy ferritic steel, whereas in the two austenitic steels, the presence of water increased chromium diffusion to the oxide scale rather than the scale thickness. The oxide layers characterized and analyzed in this paper will be further studied in terms of their abilities to resist corrosion by exposing them under corrosive conditions. The results regarding the corrosion resistance of the steels will be published in a sequel paper.

Keywords Pre-oxidation · High-temperature oxidation · Low alloy ferritic steel · Austenitic stainless steel · High alloy austenitic stainless steel

✉ J. Lehmusto
juho.lehmusto@abo.fi

D. Lindberg
daniel.lindberg@abo.fi

P. Yrjas
patrik.yrjas@abo.fi

L. Hupa
leena.hupa@abo.fi

[1] Johan Gadolin Process Chemistry Centre, Abo Akademi University, Piispankatu 8, 20500 Turku, Finland

Introduction

The increasing global power demand together with decreasing reservoirs of fossil fuels has generated growing interest in the use of more sustainable and ecological fuel sources such as waste-derived fuels and biomass. Albeit these fuels have turned out to be promising renewables for power production through combustion, they have characteristics that make them more challenging to utilize compared to traditional solid fuels such as coal. The biomass- and waste-derived fuels may contain considerable amounts of potassium, sodium, zinc, lead, and chlorine, which all are known to create fly ash with a low melting point, resulting in ash adhesion to the heat-transfer surfaces, for instance, the superheater tubes [1–3]. In addition to the loss of heat-transfer efficiency, these ash deposits cause slagging and fouling, which may lead to corrosion of the superheater tubes and at its worst, to unscheduled shutdowns of the power plant. Due to the more corrosive nature of the flue gasses and fly ash resulting from the combustion of renewables, biomass- and waste-fired boilers are set to operate at lower steam temperatures than coal-fired boilers. For example, in straw-fired boilers, maximum steam temperatures are commonly between 450 and 485 °C, depending on the composition of the superheater steel [4], as compared to 560–600 °C in coal-fired boilers. Since the oxidation or corrosion rate increases as a function of temperature, lower steam temperatures, and thus, lower surface temperatures of the superheater tubes are applied to reduce corrosion. Unfortunately, lower steam temperatures also lead to lower power production efficiency: as a rule of thumb, every 10 °C rise in the steam temperature results in an increase of approximately 2% in the power production efficiency. Therefore, more efficient ways to prevent corrosion are needed so that power plants using biomass- and waste-derived fuels can operate at higher steam temperatures.

There are several possibilities to improve materials' ability to withstand high-temperature corrosion, for example; the use of higher alloyed steels, the utilization of diffusion and overlay coatings, and the introduction of reactive elements such as yttrium and hafnium in the steel. In order to increase corrosion resistance through alloy modification, higher concentrations of chromium and nickel are required. However, the use of such high-alloyed steels increases the material costs remarkably: the relative prices per kilogram for the three commercial steels studied in this paper are 3 for the low alloy ferritic 10CrMo9-10 steel, 8.5 for the austenitic AISI 347 stainless steel, and 28 for the high alloy austenitic Sanicro 28 stainless steel [5]. So, going for even higher chromium and nickel concentrations in the steel would result in too high expenses. In addition, certain Fe–Cr–Ni alloys were originally designed for aqueous environments, making their corrosion resistance properties less suitable for high-temperature environments [6]. The drawback of using diffusion and overlay coatings in boiler environments lies in their susceptibility to cyclic temperature profiles, which repeatedly occur in boilers due to maintenance shutdowns. Another frailty of the coatings is the limited reservoir of the scale-forming elements, which may result in a defective corrosion protection during sufficiently long operation period of the boiler. In the case of chromia formers, the positive effect of the reactive element addition on the formation of the protective oxide scale is small at temperatures below 900 °C [7]. Since the typical

material temperature of the superheater tubes in boilers firing biomass lies around 550 °C, the introduction of reactive elements would not increase protective oxide scale formation in a desirable way.

In the case of pure iron and at temperatures below 570 °C, the formed scale consists of two different iron oxides: magnetite (Fe_3O_4) closest to the metal, followed by hematite (Fe_2O_3) as the outermost oxide layer [8]. Above 570 °C, the formed scale consists of three different iron oxides: wüstite (FeO) forming next to the metal, followed by magnetite and finally, hematite as the outermost oxide layer. Although small amounts of chromium alloyed with iron result in improved hardenability and strength of the steel rather than in increased ability to resist corrosion, low-alloyed steels are used in boiler sections with a less corrosive environment and lower steel temperature. In this study, the low alloy ferritic 10CrMo9-10 steel represents this category. As the chromium content increases, the thickness of iron–chromium spinel oxide increases at the same time as the wüstite layer becomes thinner, due to the blockage of Fe^{2+} ions by the formed spinel [6]. Finally, with high enough chromium concentrations, a mixed Fe–Cr spinel with an initial outer layer of pure Cr_2O_3 is formed. The Nb-stabilized AISI 347 and the high alloy Sanicro 28 austenitic stainless steels belong to this category.

Instead of improving superheater material durability using expensive superalloys, manipulating the protective properties of the already existing alloys through pre-oxidation may offer cost-effective possibilities for corrosion prevention. So far, the reported results are encouraging: the pre-oxidation has been reported to give a beneficial effect regarding corrosion resistance toward a corrosive salt in the case with an alumina-forming steel [9] or toward high-temperature pitting corrosion in the case with a chromium-forming steel [10].

The aim of this two-part study is to investigate the connection between the heat treatment conditions prior to the exposure and the corrosion resistance of the steels when exposed to detrimental potassium chloride. This first part reported here focuses on the oxidation behavior of three commercial superheater steels under various conditions, whereas the second part, which will be published in a sequel paper, will address the corrosion resistance of the pre-oxidized steels.

Experimental Procedures

The commercial steels of interest were a low alloy ferritic 10CrMo9-10 steel, a Nb-stabilized austenitic AISI347 steel, and a high alloy austenitic Sanicro 28 steel (Table 1). All three steels are used in power plants, where the choice of steel grade

Table 1 Chemical compositions of steels in wt%

Steel	Cr	Fe	Mn	Mo	Ni	Si	Others
10CrMo9–10	2.3	93.4	0.8	1.0	–	0.3	
AISI347	17.7	68.2	2.1	–	8.5	0.4	Nb 1.5
Sanicro 28	25.9	35.9	2.0	3.4	29.2	0.5	Cu 1.2

is determined, among other factors, by the aggressiveness of the environment and by steam and flue gas temperatures.

The samples were cut from genuine superheater tubes; the surface area of each sample was 4 cm^2 (2 cm × 2 cm) and the thickness 0.5 cm. Prior to high-temperature exposures, the steel samples were polished in water with a 280 grit SiC grinding paper, followed by polishing in ethanol with a 500 grit SiC grinding paper. The samples were further cleaned in ethanol using an ultrasonic bath. High-temperature exposures were carried out in a temperature-controlled horizontal tube furnace, where the temperature was measured with thermocouples installed between adjacent samples and at both ends of the sample holder. The sample temperatures were within ±5 °C of the target temperature, and the heating rate was 5 °C min^{-1}. In order to minimize the effect of ambient humidity during the dry exposures, the samples were positioned inside a sealed quartz reactor, through which synthetic air (21% O$_2$, 79% N$_2$) was passed with a flow rate of 400 ml min^{-1}. The humid exposures contained 10% water vapor, which was created by injecting (Braun Perfusor Compact S) water into a preheater, from where the evaporated water was introduced into the tube furnace. The samples were positioned horizontally, parallel to the direction of the gas flow. The warm-up and cool-down periods were carried out in the same atmosphere as the exposures. The dry exposures were run at 200, 500, or 700 °C, with two different exposure times: 5 and 24 h. The exposures under humid conditions were carried out at 500 °C for either 5 or 24 h. A reference sample of each steel was also cleaned and polished, but these samples were not heat-treated in any way.

After the exposures, the samples were allowed to cool to room temperature in the synthetic air inside the quartz reactor and were then analyzed. Regarding the humid exposures, the water supply was discontinued together with the furnace shutdown. The thicknesses and the depth profiles of the formed oxide scales were measured with X-ray Photoelectron Spectroscope (XPS, Physical Electronics Inc. Quantum 2000) by sputtering the oxide scales with Ar-beam. The beam diameter was 100 μm, the voltage was 5 kV and the sputtering area either 1 mm^2 (1 × 1 mm) or 9 mm^2 (3 × 3 mm). After the XPS measurements, Multipak 9.0 software was used to analyze the oxide scale compositions. In the case of the ferritic steel samples exposed at 700 °C, the formed oxide scales were too thick to be analyzed with XPS. Therefore, the samples were cast into chlorine-free polyester casting resin (EliChem Resins Ltd.), cut and polished for cross-sectional EDX analyses. The sample surfaces, especially their morphologies and chemical compositions, were studied with scanning electron microscope (LEO 1530 Gemini) coupled to X-ray detector (Thermo Scientific UltraDry Silicon Drift Detector) and energy dispersive X-ray analysis system (Thermo Scientific ThermoNORAN Vantage X-ray). The microscope was operated at an accelerating voltage of 2.7 kV for general imaging, 15 kV for spot and area analyses, and 20 kV for EDX analyses. The backscattered electron mode was used for the images affiliated with the EDX analyses, while the InLens mode (a secondary electron mode also known as Through The Lens mode) was applied for detailed structural images of the formed oxide scales viewed from above.

Table 2 Components of the stable solid solution phases. Mn-containing spinel was used for the 10CrMo9-10 steel, and Ni-containing spinel was used for the AISI347 and Sanicro 28 steels

	Components	Database
Oxide phase		
Spinel	$(Fe,Cr,Ni)(Fe,Cr,Ni,Va^*)_2O_4$ (main components Fe_3O_4–$NiFe_2O_4$–$FeCr_2O_4$)	FToxid
	$(Fe,Cr,Mn)(Fe,Cr,Mn,Va^*)_2O_4$	
	(main components Fe_3O_4–$MnFe_2O_4$–$MnCr_2O_4$–$FeCr_2O_4$)	
$(Fe,Cr)_2O_3$ (corundum)	$(Fe,Cr,Mn)_2O_3$	FToxid
MeO	$(Fe,Mn,Ni)O$	FToxid
Bixbyite	$(Mn,Cr,Fe)_2O_3$	FToxid
Alloy phase		
BCC_A2	$(Cr,Cu,Fe,Mn,Mo,Nb,Ni,O,Si)Va^*$	SGTE alloy
FCC_A1	$(Cr,Cu,Fe,Mn,Mo,Nb,Ni,O,Si)Va_3^*$	SGTE alloy
Mu(μ) phase	$(Cr,Fe,Ni)_7(Mo,Nb)_2(Cr,Fe,Nb,Ni)_4$	SGTE alloy
Sigma(σ) phase	$(Fe,Mn,Ni)_8(Cr,Mo)_4(Cr,Fe,Mn,Mo,Ni)_{18}$	SGTE alloy
Laves phase	$(Fe,Cr)_2(Mo,Nb)$	
Cr_3Si	$(Cr,Si)_3(Si,Cr)$	

* Va is a vacancy in the sub-lattice of a phase

Thermodynamic equilibrium modeling was used to predict the oxidation behavior of the studied steels. In the present study, the main interest was to predict the elemental distribution in the alloy and oxide phases as a function of $p(O_2)$ under the conditions where both alloy phases are in equilibrium with oxide phases (corrosion products). The aim was to distinguish the different oxidation behavior of the three steels, especially in what order the different alloying elements are oxidized as a function of increasing oxygen activity.

The calculations were performed with the thermodynamic software package Factsage 6.4 [11] using a custom selected thermodynamic database based on the existing FactPS (pure substance) database for stoichiometric solid and liquid phases and the gas phase, the FToxid database for oxide solid and liquid solutions, as well as the SGTE alloy database for the main and minor alloy phases. The components of the main oxide and alloy phases that are stable in the predictions are given in Table 2.

The calculations were performed for conditions with constant temperature (500 and 700 °C) and constant total pressure (1 bar) with varying $p(O_2)$ from $\log_{10} p(O_2) = -50$ to $\log_{10} p(O_2) = 0$ (1 bar O_2) with steps of 0.2 on the logarithmic scale. Input for the steel compositions was taken from Table 1.

The experimental case with water vapor present was not predicted as the relation between the $p(O_2)$ and $p(H_2O)$ gradient close to the alloy/oxide interface is difficult to estimate.

Results

Oxide Scale Thickness

XPS was used to measure the oxide scale thicknesses. The evaluation of the scale thickness is based on plotting the measured intensities of chosen elements as a function of sputter time, which is then converted to sputtered depth. First, the sputter rate of the instrument was determined by sputtering through a 100-nm-thick SiO_2 standard. The sputtering times were 42 and 312 s for areas of 1 and 9 mm^2, respectively. Compared to the sputter rate in SiO_2, a conversion coefficient of 0.61 has been measured for Fe_2O_3 [12], 0.54 for Cr_2O_3 [12], and 0.75 for NiO [13]. The conversion coefficient for NiO has been assumed the same as the coefficient for Ta_2O_5, which is 0.75 [13]. Based on these coefficients, all the measured sputtering times were converted to approximate oxide scale thicknesses and are presented in Table 3. The oxide scale was considered to be pierced once the intensity of the oxygen signal was half of the initial signal. Since the oxide scales formed on Cr-containing steels at room temperature consist of mainly chromium, the conversion coefficient for pure Cr_2O_3 has been used in the case of the reference samples [14]. For the other samples, the conversion coefficient was chosen on grounds of the chemical composition of the formed oxide scale, identified with XPS. If the oxide scale consisted of several oxides, the average of relevant coefficients was used.

Oxide Scale Composition and Structure

The results have been divided primarily according to the steel type and secondarily according to the analysis method. The oxide scales on the reference samples were so thin that their chemical compositions could not be determined from the XPS data. However, thin oxide scales formed on Cr-containing steels at room temperature have been reported to consist of chromium hydroxide in the outermost layer and chromium oxide in the inner layer [15].

Table 3 Measured approximate oxide scale thicknesses after the high-temperature treatments

Approximate oxide scale thickness (nm)			
Conditions	10CrMo9-10	AISI347	Sanicro 28
Reference	18	12	7
5 h at 200 °C	17	7	3
24 h at 200 °C	20	8	4
5 h at 500 °C	800	22	30
5 h at 500 °C (humid)	1600	22	31
24 h at 500 °C	2800	24	42
24 h at 500 °C (humid)	4600	22	39
5 h at 700 °C	>20 μm*	93	120
24 h at 700 °C	>20 μm*	629	184

* Measured from the cross-sectional sample imaged with SEM

Low Alloy Ferritic Steel

Depth Profile According to the XPS measurements and EDX analyses of the low alloy ferritic steel samples, the oxide scales formed under all test conditions consisted mostly of pure iron oxide, with a chromium enrichment close to the oxide/steel interface (Fig. 1). In addition, minor differences in the oxide scale structure could be observed from the cross-sectional SEM images (Fig. 2). The oxide scale after 5 h at 700 °C appeared dense, whereas cavities were observed within the oxide scale after 24 h at 700 °C. Moreover, the oxide scale after 5 h at 700 °C was
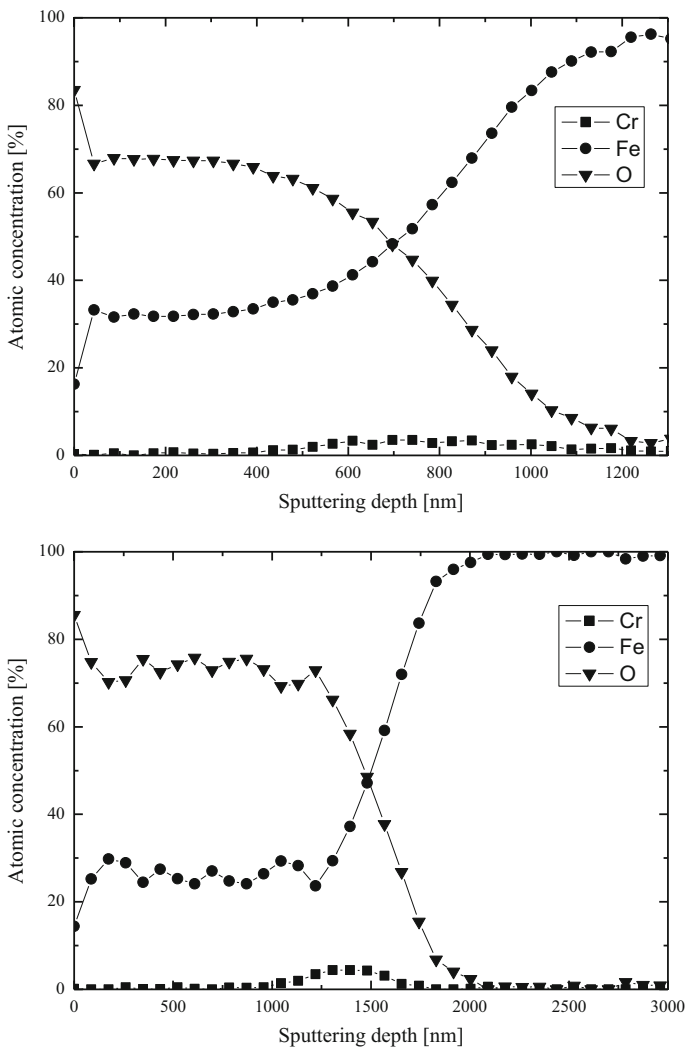
Fig. 1 Depth profiles of the low alloy ferritic 10CrMo9-10 steel sample after being exposed to 500 °C for 5 h under dry (*upper*) and humid (*lower*) conditions

detached from the bulk material, whereas the oxide scale formed during the longer exposure time remained attached to the bulk material.

Surface Structure   SEM images did not reveal any structural details such as oxide nuclei or layer on the surface of the low alloy reference sample (Fig. 3a). The area analyses of the reference sample and the sample oxidized for 5 h at 200 °C gave the same results, the nominal composition of the steel. However, oxide nuclei with a diameter of around 50 nm were seen on the thermally treated sample, forming line-like structures on the surface (indicated by an arrow in Fig. 3b). After the 24-h exposure time, a slight decrease of the chromium content compared to the nominal bulk composition was measured, whereas the iron content was slightly higher. Also, the network of the line-like structures, presumably along the surface grain boundaries, was more continuous along the surface with a nucleus diameter of around 30 nm (Fig. 3c). In addition, separate nuclei with a diameter of around 40 nm had formed on the surface (a group of these is marked with a circle in Fig. 3c).

When the exposure temperature under dry conditions was increased to 500 °C, the iron content in the oxide scale increased further with respect to the chromium content after 5 h. The surface was covered with a continuous, yet porous iron oxide consisting of whiskers pointing out (Fig. 3d, the whiskers are difficult to see due to the image size). The presence of water did not alter the chemical composition of the surface, but the oxide scale was more porous and consisted of iron oxide flakes (Fig. 3e). The longer exposure time, 24 h at 500 °C under dry conditions resulted in a continuous chromium-free, yet porous iron oxide with remarkably more whiskers compared to the samples exposed for 5 h only (Fig. 3f). After 24 h, the presence of water resulted in a surface completely covered with iron oxide flakes with traces of chromium (Fig. 3g).

At the highest exposure temperature, 700 °C, the amount of chromium in the surface layer was about the same as in the sample exposed to 500 °C for 24 h under humid conditions. The whisker-rich surface structure present at 500 °C has changed into a highly porous surface consisting of iron oxide grains (Fig. 3h). Virtually no chromium could be detected in the oxide scale after the longer exposure time at
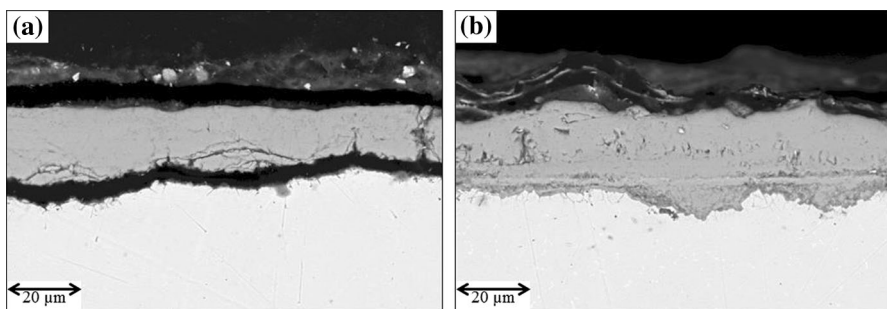

Fig. 2 Cross-sectional images of the low alloy ferritic 10CrMo9-10 steel sample at 700 °C after **a** 5 h, **b** 24 h
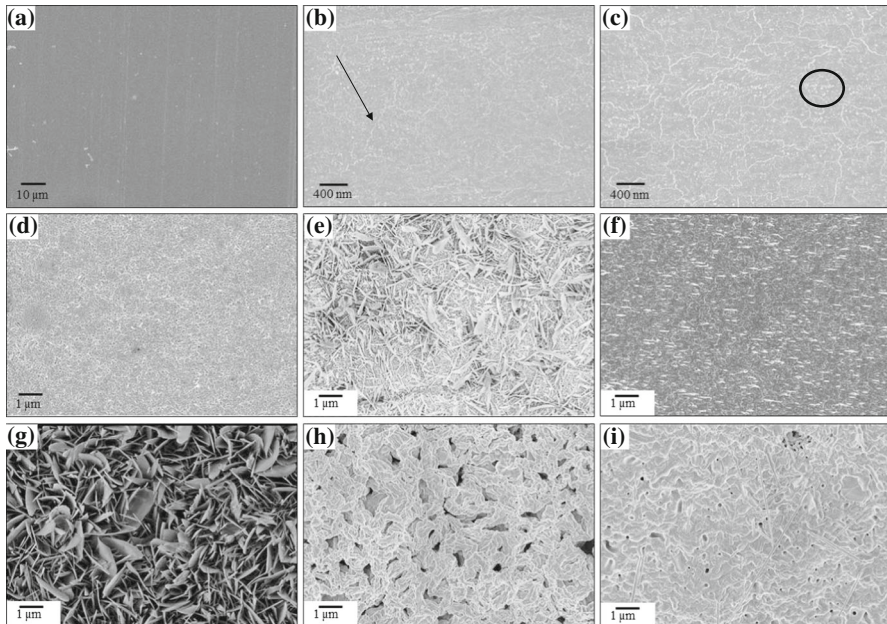
Fig. 3 InLens-images of the low alloy ferritic 10CrMo9-10 steel surfaces at dry and humid conditions. **a** reference, **b** 5 h at 200 °C, dry (the *arrow* indicates the oxide nuclei along a grain boundary), **c** 24 h at 200 °C, dry (the *circle* indicates a group of separate oxide nuclei), **d** 5 h at 500 °C, dry, **e** 5 h at 500 °C, humid, **f** 24 h at 500 °C, dry, **g** 24 h at 500 °C, humid, **h** 5 h at 700 °C, dry, **i** 24 h at 700 °C, dry

700 °C, and the sample surface was similar to the sample exposed for 5 h with both porous and needle-like iron oxide grains (Fig. 3i).

Thermodynamic Predictions The BCC phase is predicted to be the main phase with less than 1 wt% Laves phase under the pre-oxidation conditions for the 10CrMo9-10 alloy. The predicted oxidation of the ferritic steel at 500 °C as a function of p(O$_2$) starts with the oxidation of Mn and Si to Mn-silicates and SiO$_2$, followed by oxidation of Cr to a spinel phase, initially as MnCr$_2$O$_4$-rich spinel, followed by FeCr$_2$O$_4$ formation. Subsequently, the bulk of Fe in the steel is oxidized and the spinel phase is mainly Fe$_3$O$_4$-rich. Finally, Mo is oxidized to MoO$_2$. The steel composition changes to almost pure Fe metal as the oxidation proceeds. The oxidation order of the metals is Mn, Si → Cr → Fe → Mo. The oxidation sequence is similar at 700 °C, with the difference that wüstite is predicted to form at a very narrow p(O$_2$) range when the main Fe oxidation proceeds with formation of Fe$_3$O$_4$-rich spinel. At high p(O$_2$), the stable oxide phase is hematite dissolving minor amounts of Cr ((Fe,Cr)$_2$O$_3$(ss)). Figures 4 and 5 show the predicted phase equilibria of the 10CrMo9-10 alloy at 500 and 700 °C as functions of p(O$_2$), as well as the overall elemental compositions of the oxide and alloy phases.
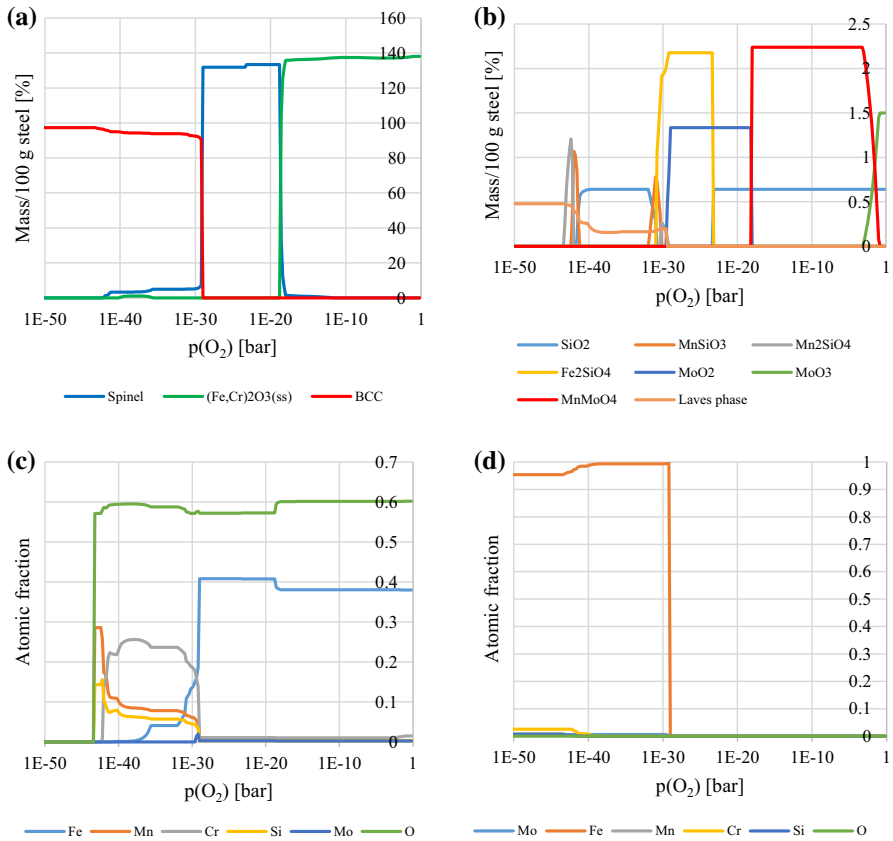
Fig. 4 Predicted phase equilibrium of the 10CrMo9-10 alloy at 500 °C as a function of p(O$_2$): major phases (**a**), minor phases (**b**), and the elemental composition of the oxide (**c**) and alloy phases (**d**)

Nb-Stabilized Austenitic AISI347 Steel

Depth Profile The chemical composition of the oxide scale on the Nb-stabilized austenitic steel at 200 °C was similar after both exposure times: an oxide scale with an iron-rich outer layer and a chromium-rich inner layer, in which the chromium content did not surpass the bulk concentration of chromium (Fig. 6). Right below the duplex Fe–Cr oxide, a Ni-enriched region was detected.

The duplex structure of the oxide scale became more pronounced when the samples were exposed at 500 °C to both dry and humid conditions. After 5 h at 500 °C in dry air, the chromium content was higher in the oxide scale than in the bulk material, whereas the iron content of the oxide scale did not surpass the iron content of the bulk material (Fig. 7a). Nickel enrichment below the oxide scale could not be detected clearly, nor was there any variation in niobium concentration. A similar duplex oxide structure was formed in the presence of water; the iron content of the outermost layer of the oxide scale nearly equaled the iron content of the bulk material, whereas the chromium content of the inner layer of the oxide
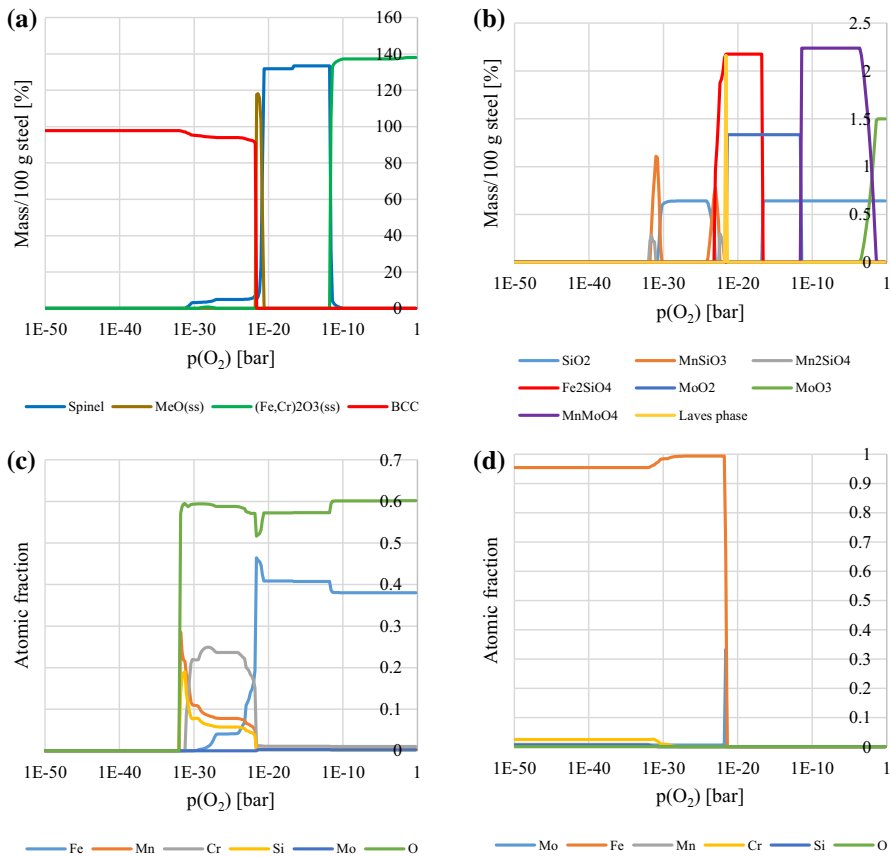
(a)

(b)

(c)

(d)

Fig. 5 Predicted phase equilibrium of the 10CrMo9-10 alloy at 700 °C as a function of p(O₂): major phases (**a**), minor phases (**b**), and the elemental composition of the oxide (**c**) and alloy phases (**d**)

scale surpassed that of the bulk material (Fig. 7b). Additionally, a region depleted in chromium and enriched with manganese was found below the oxide scale, but no clear Ni-enrichment could be detected. Again, the Nb-content remained unaltered throughout the depth profile. After 24 h at 500 °C in dry air, both the iron-rich outer layer and the chromium-rich inner layer of the oxide scale were thicker. Otherwise, the oxide scale was similar to the one formed at 500 °C in 5 h. Both layers of the scale were thicker under humid conditions with an iron content nearly equaling the bulk content together with a chromium content surpassing the bulk content. The chromium-depleted region below the oxide scale could still be identified, but neither Mn- or Ni-enrichments nor variations in the Nb-content were observed.

A surface layer of almost pure chromium oxide was measured after 5 h at 700 °C. The outermost layer of the oxide scale also contained manganese more than in the bulk material. Neither Ni-enrichment nor Cr-depletion was measured below the oxide scale. Also, the Nb-content remained unaltered. After the longer exposure time, no manganese was found in the oxide scale, which now consisted solely of
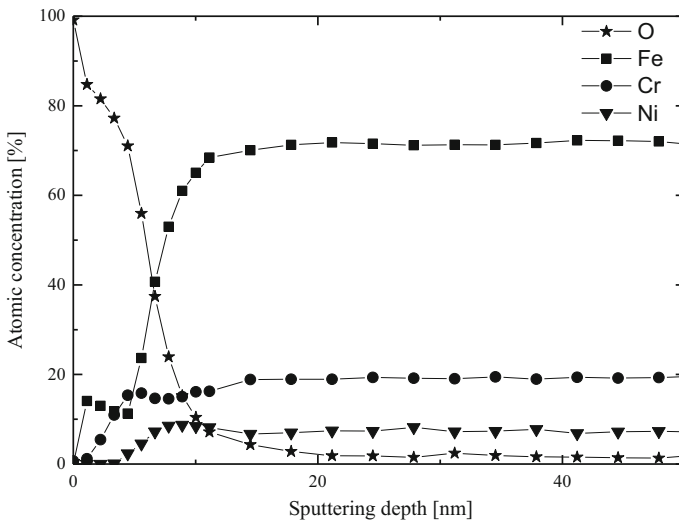
Fig. 6 Depth profile of the Nb-stabilized austenitic AISI347 steel sample after 24 h at 200 °C

chromium. The region below the oxide scale was similar to the one formed in 5 h no changes of Mn-, Ni-, Cr- or Nb-content compared to the bulk material.

Surface Structure SEM images of the reference sample did not show any structural details such as oxide nuclei or layer (Fig. 8a). According to the area analysis, the compositions of the reference sample and the sample exposed to 200 °C corresponded to the nominal composition of the steel. However, with a higher magnification, separate oxide nuclei roughly 30 nm in diameter could be observed on the steel surface after the 5 h exposure (Fig. 8b, the oxide nuclei are not visible here). The oxide nuclei had not grown in size after the longer exposure time, but their number had increased (Fig. 8c). Despite the increased amount of nuclei, the surface was not yet fully covered by them.

At 500 °C under dry conditions, nodules with dimensions of a few microns were seen on the surface after 5 h (indicated by a circle in Fig. 8d). The appearance of these nodules suggests that they originate from bursts through the surface. According to SEM analyses, these nodules consisted of following elements in weight percent (bulk amounts are displayed in brackets for comparison): Cr 10.3 (17.7); Mn 0.6 (2.1); Fe 31.9 (68.2), Ni 4.1 (8.5), Nb 28.3 (1.5). In addition to the Nb-rich nodules, another type of local failure was observed on the surface: the material has partly been depleted along the grain boundaries, leaving separate grains clearly visible (Fig. 9). Excluding these local failures, a more continuous oxide layer with the outlines of separate oxide nuclei (roughly 50 nm in diameter) was still to be seen (Fig. 9). Compared to the dry conditions, the introduction of water vapor did not change the layer structure or its composition significantly: the Nb-rich nodules appeared to be somewhat smaller (dimensions 1 micron), but the oxide nuclei were slightly bigger (diameter >50 nm) (Fig. 8e). The above-
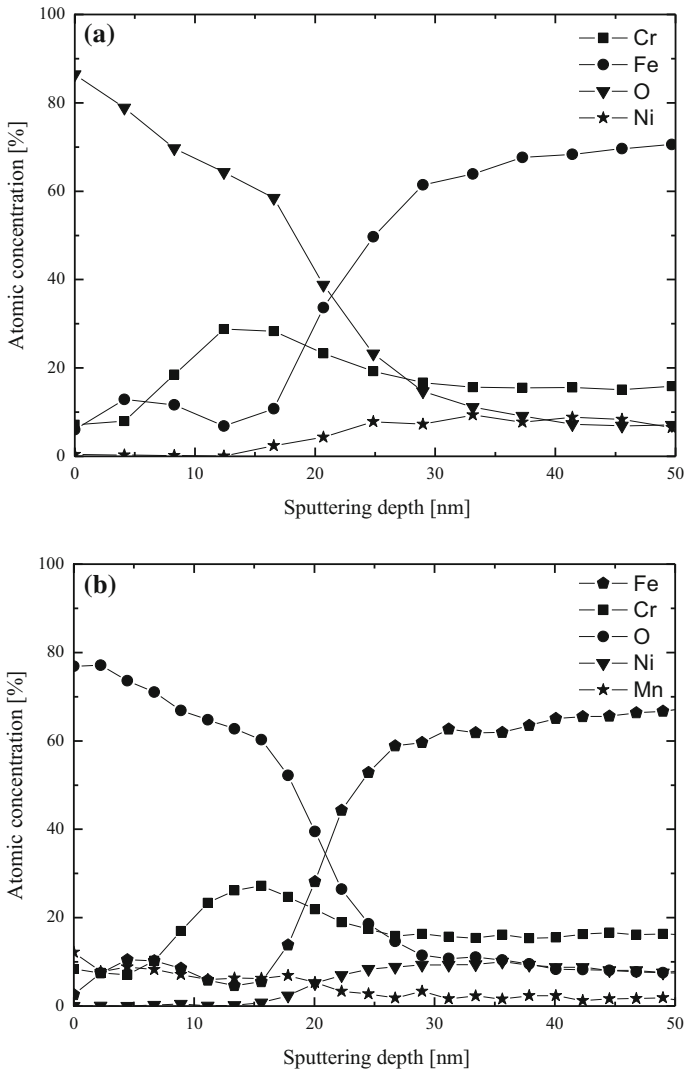
Fig. 7 Depth profiles of the Nb-stabilized austenitic AISI347 steel sample after 5 h at 500 °C under **a** dry and **b** humid conditions

mentioned grain boundary corrosion was also detected, but it was not as enhanced as in the dry air. Apart from an increased Ni-content at the surface, the 24-h exposure under dry conditions did not alter the chemical composition of the surface compared to the bulk material. Again, Nb-rich structures with up to 40 wt% niobium were detected on the surface (Fig. 8f). The size of these nodules was similar to the one found in the 5-h exposure, while the material degradation along the grain boundaries appeared far more pronounced. The introduction of water increased the Ni-content in the vicinity of the surface, the Nb-rich nodules still
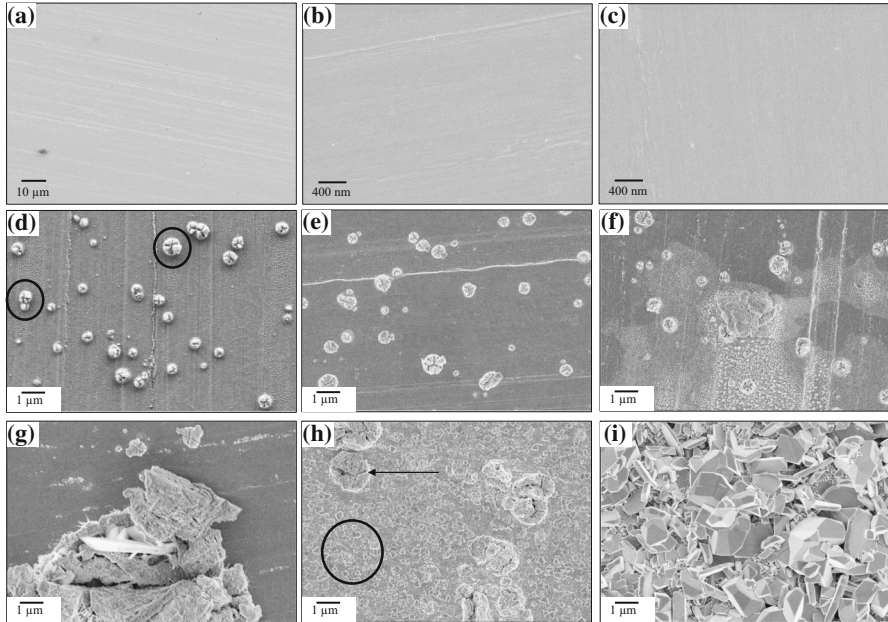
Fig. 8 InLens-images of the Nb-stabilized austenitic AISI347 steel surfaces at dry and humid conditions. **a** reference, **b** 5 h at 200 °C, dry, **c** 24 h at 200 °C, dry, **d** 5 h at 500 °C, dry (the *circles* indicate the formed Nb-rich nodules), **e** 5 h at 500 °C, humid, **f** 24 h at 500 °C, dry, **g** 24 h at 500 °C, humid, **h** 5 h at 700 °C, dry (the *arrow* indicates a Nb-rich structures and the circle a group of formed Cr_2O_3 crystals), **i** 24 h at 700 °C, dry
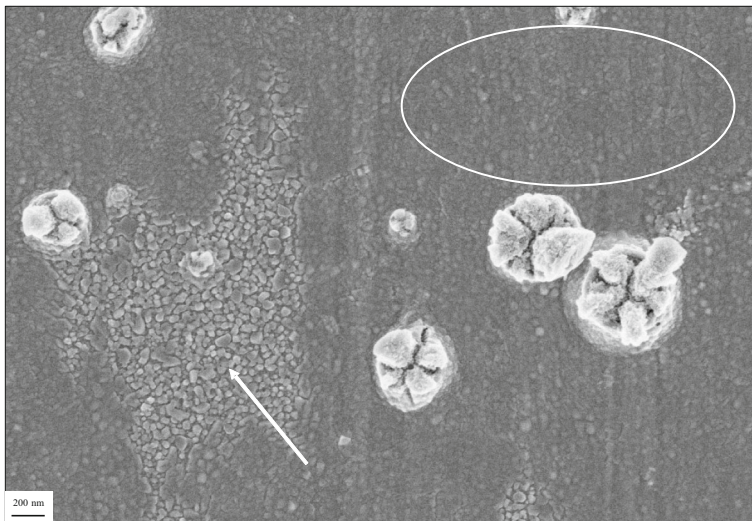

Fig. 9 InLens-image of the Nb-stabilized austenitic AISI347 steel surface after 5 h at 500 °C in dry conditions. The *arrow* indicates an area with material depletion along the grain boundaries, the *oval marks* an area of a more continuous oxide layer with the outlines of separate oxide particles

forming on the surface. The nodules had partly broken down, exposing the inner steel to oxygen and resulting in local corrosion producing iron and chromium oxides (Fig. 8g). Virtually no material depletion along the grain boundaries could be observed at the surface of the analyzed sample.

At 700 °C under dry conditions, the Cr- and Mn-contents in the oxide scale were slightly higher than in the bulk material. Nodules with roughly 30 wt% of Nb, 6 wt% of Mn, and less than 2 wt% of Ni were observed on the surface (Fig. 8h). Excluding these nodules, the surface was relatively homogeneously oxidized resulting in bigger chromium oxide particles (<400 nm, indicated with a circle in Fig. 8h). The 24-h exposure at 700 °C resulted in a surface, where the Nb-rich nodules could no longer be observed as the surface was completely covered with chromium oxide crystals bigger than a micron (Fig. 8i). The size variation of the crystals was larger when compared to the shorter exposure time at 700 °C. The surface contained 28 wt% of Cr and 4 wt% of Mn according to a general area analysis.

Thermodynamic Predictions   The austenitic AISI347 alloy consists mainly of an FCC phase. However, the thermodynamic equilibria at 500 and 700 °C predict a mixture of BCC, FCC and minor amounts of the Laves phase. The predicted oxidation of the austenitic AISI347 alloy at 500 °C as a function of $p(O_2)$ starts with the oxidation of Mn and Si to Mn-silicates and SiO_2, followed by oxidation of Cr to a Cr_2O_3 and Nb to NbO, NbO_2 and Nb_2O_5. Subsequently, Fe is oxidized and reacts with Cr_2O_3 to form $FeCr_2O_4$ and finally Fe_3O_4. Ni is finally oxidized and dissolves into the spinel phase. At high $p(O_2)$, the stable oxide phases are $(Fe,Cr)_2O_3(ss)$ (hematite dissolving Cr_2O_3) and a spinel, rich in $NiFe_2O_4$ and minor amounts of chromium components. The steel composition changes to a Fe/Ni mixture and finally pure Ni as the oxidation proceeds. The oxidation order of the metals is Mn, Si → Cr, Nb → Fe → Ni. The oxidation sequence is similar at 700 °C. Figures 10 and 11 show the predicted phase equilibria of the AISI347 alloy at 500 and 700 °C as functions of $p(O_2)$, as well as the overall elemental compositions of the oxide and alloy phases.

High Alloy Austenitic Sanicro 28 Steel

Depth Profile   A thin oxide scale with an iron-rich outer layer, followed by a chromium-rich inner layer formed on the high alloy austenitic steel after both exposure times at 200 °C. Ni- and Fe-enrichments were found under the duplex oxide, exceeding the bulk concentration of both nickel and iron. However, the chromium in the oxide scale did not surpass the bulk concentration of chromium.

A similar duplex oxide with a thin iron-rich outer layer, followed by a chromium-rich inner layer formed in 5 h at 500 °C under dry conditions (Fig. 12a). The thickness of the Cr-rich layer of the oxide scale was roughly four times the thickness of the Fe-rich layer. In contrast to the lower exposure temperature, no Ni-enrichment could be observed below the duplex scale. The presence of water altered the oxide scale composition slightly, although the duplex oxide with a very thin
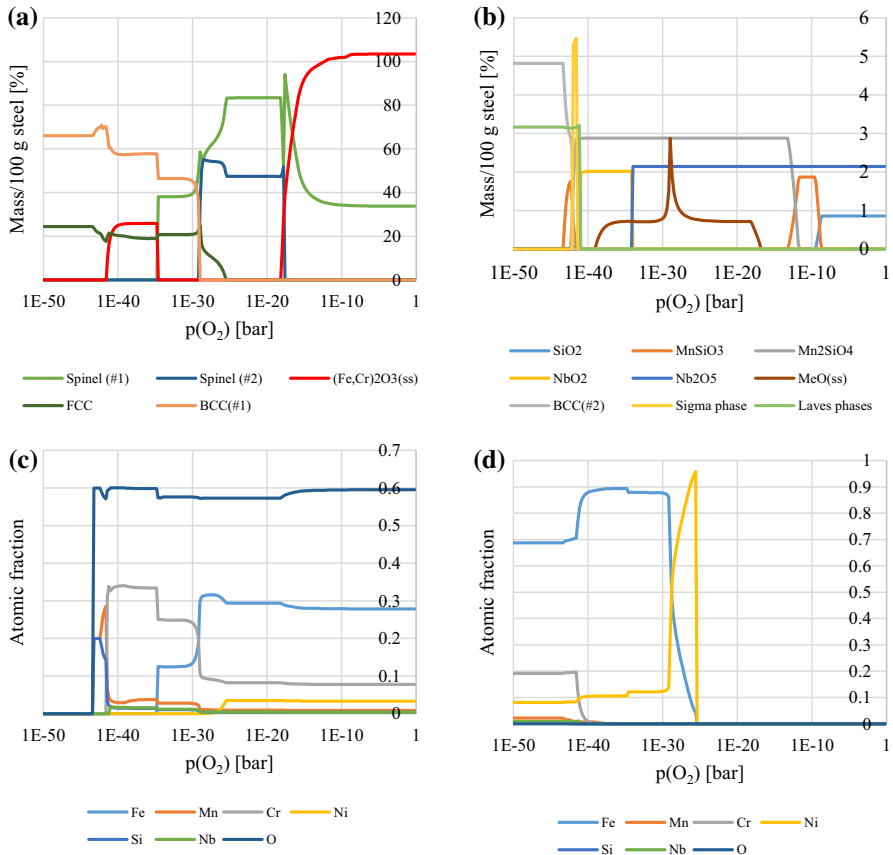
Fig. 10 Predicted phase equilibrium of the AISI347 alloy at 500 °C as a function of p(O$_2$): major phases (**a**), minor phases (**b**), and the elemental composition of the oxide (**c**) and alloy phases (**d**)

outer Fe-rich layer followed by a Cr-rich layer formed, Ni- and Mn-enrichments together with Cr-depletion could be detected underneath the oxide scale (Fig. 12b). The longer exposure time under dry conditions resulted in a very similar duplex oxide with no element enrichments below it, as was observed at 500 °C after the shorter exposure time. The only difference was the ratio between the thicknesses of Fe-rich and Cr-rich layers of the oxide scale. The Cr-rich layer was now roughly five times thicker than the Fe-rich layer. Again, the presence of water altered the oxide scale composition only slightly. Ni- and Mn-enrichments together with Cr-depletion could be detected underneath the duplex oxide consisting of a very thin Fe-rich outer layer, followed by Cr-rich inner layer.

During both exposure times, a virtually Fe-free oxide scale, mostly consisting of chromium with a Mn-rich outermost layer formed at 700 °C. Underneath the oxide scale, a region with Ni-enrichment together with Cr-depletion was detected.
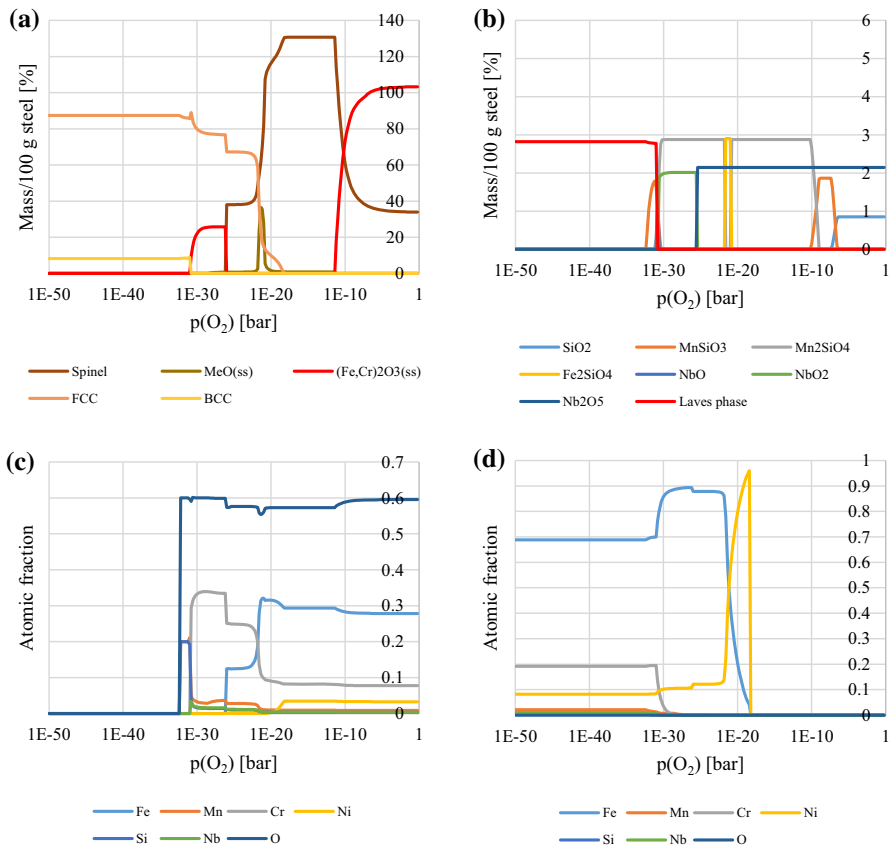
Fig. 11 Predicted phase equilibrium of the AISI347 alloy at 700 °C as a function of p(O$_2$): major phases (**a**), minor phases (**b**), and the elemental composition of the oxide (**c**) and alloy phases (**d**)

Surface Structure   No structural details such as oxide nuclei or layer could be detected in the SEM micrographs of the reference surface (Fig. 13a). The area analysis corresponded to the nominal composition of the steel, as it did for the samples exposed at 200 °C (Figs. 13b, c). In addition, no fine structure such as oxide nuclei could be observed at the surfaces, even when 50,000-fold magnification was used.

Small amounts of oxygen (2 wt%) could be measured at the surface of the sample exposed for 5 h at 500 °C under dry conditions, but otherwise the surface composition was the same as in bulk material. The surface was homogeneously covered with small (<100 nm) oxide grains (Fig. 13d). The amount of detected oxygen at the surface did not alter in the presence of water, nor did the amount of elements when compared to the bulk composition. The surface was homogeneously covered with oxide grains, which were smaller (<50 nm) than those formed under dry conditions (Fig. 13e).
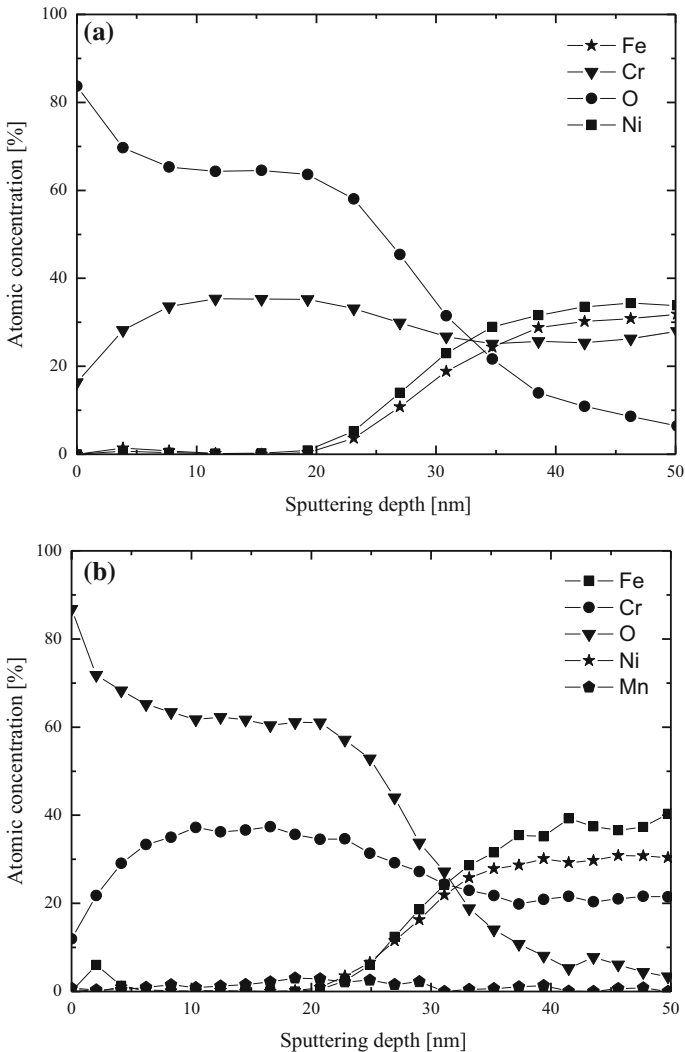
Fig. 12 Depth profiles of the high alloy austenitic Sanicro 28 steel after 5 h at 500 °C under **a** dry and **b** humid conditions

At prolonged exposure, the oxide nuclei grew bigger and local island structures could be seen at the surface (Fig. 13f). The oxygen content was slightly higher (6 wt%) at these locations when compared to the overall surface (3–4 wt%), but no clear difference in other element concentrations could be observed: the structures were too thin to be analyzed with greater certainty. In the presence of water, larger (around 400 nm) separate chromia crystals grew on top of the homogeneously covered surface (Fig. 13g). Again, a small amount of oxygen (3 wt%) was detected at the surface, but no depletion or enrichment of metals could be observed.
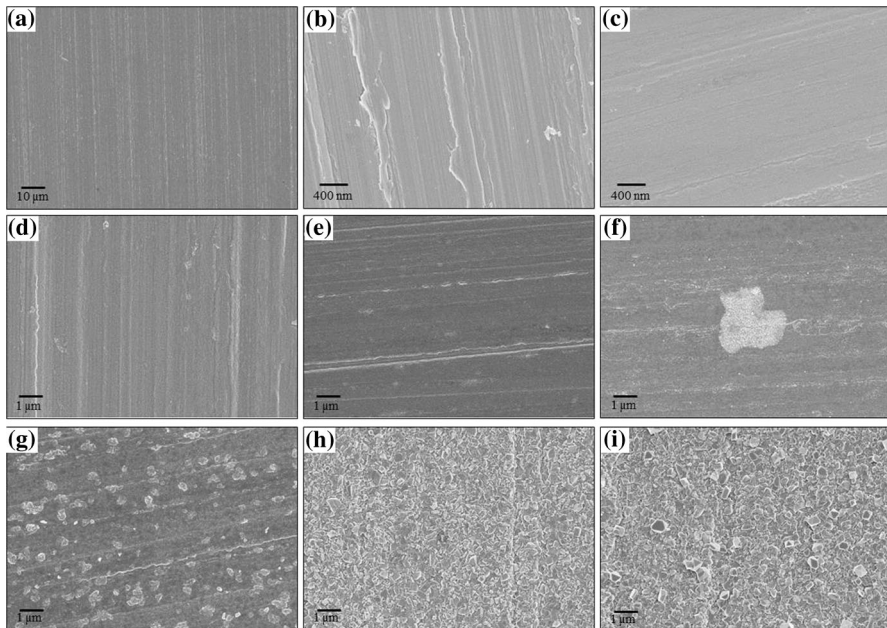
Fig. 13 InLens-images of the high alloy austenitic Sanicro 28 steel surfaces at dry and humid conditions. **a** reference, **b** 5 h at 200 °C, **c** 24 h at 200 °C, **d** 5 h at 500 °C, **e** 5 h at 500 °C under humid conditions, **f** 24 h at 500 °C, **g** 24 h at 500 °C under humid conditions, **h** 5 h at 700 °C, **i** 24 h at 700 °C

The oxygen content of the surface increased to 9 wt% after 5 h at 700 °C, but no other changes in the elemental composition were measured. The surface was covered with chromia crystals with size variation roughly between 200 and 400 nm (Fig. 13h). Despite the grain growth of the homogeneous oxide scale, the scale appeared dense and well adhered and no spallation was observed. The longer exposure time resulted in around 12 wt% of oxygen at the surface with an increase in Cr-content together with a decrease in Ni- and Fe-contents. The largest chromia crystals were still around 400 nm, but the majority of the crystals appeared smaller than after 5 h (Fig. 13i). The oxide scale appeared dense and well adhered also after 24 h with no spallation to be observed.

Thermodynamic Predictions   The austenitic Sanicro 28 steel consists mainly of an FCC phase with minor amounts of BCC and intermetallic sigma phases. The predicted oxidation of Sanicro 28 at 500 °C as a function of $p(O_2)$ starts with the oxidation of Si to SiO_2, followed by oxidation of Mn to Mn-silicates and Cr to Cr_2O_3. Subsequently, Fe is oxidized and reacts with Cr_2O_3 to form $FeCr_2O_4$, followed by oxidation of Mo, Ni, and finally Cu. Mo initially forms MoO_2, and Ni dissolves into the spinel phase, whereas Cu forms CuO and other Cu-oxides. At high $p(O_2)$, the stable oxide phase is $Ni(Fe,Cr)_2O_4$ spinel and Cr_2O_3 dissolving minor amounts of Fe and Mn. The steel composition changes to a Fe/Ni mixture, followed by almost pure Ni and finally pure Cu as the oxidation proceeds. The oxidation

order of the metals is Si → Cr, Mn → Fe → Mo → Ni → Cu. The oxidation sequence is similar at 700 °C. Figures 14 and 15 show the predicted phase equilibria of the Sanicro 28 alloy at 500 and 700 °C as functions of p(O$_2$), as well as the overall elemental compositions of the oxide and alloy phases.

Discussion

Low Alloy Ferritic Steel

The oxidation behavior of low-alloyed Fe–Cr steels is very similar to that of pure iron, where the outer layer of the oxide scale consists of, starting from the top surface, hematite (Fe$_2$O$_3$), magnetite (Fe$_3$O$_4$), and wüstite (FeO), followed by the inner layer of the oxide scale containing an iron-chromium spinel (FeCr$_2$O$_4$) and FeO [16]. The scale structure with various iron oxides originates from two different
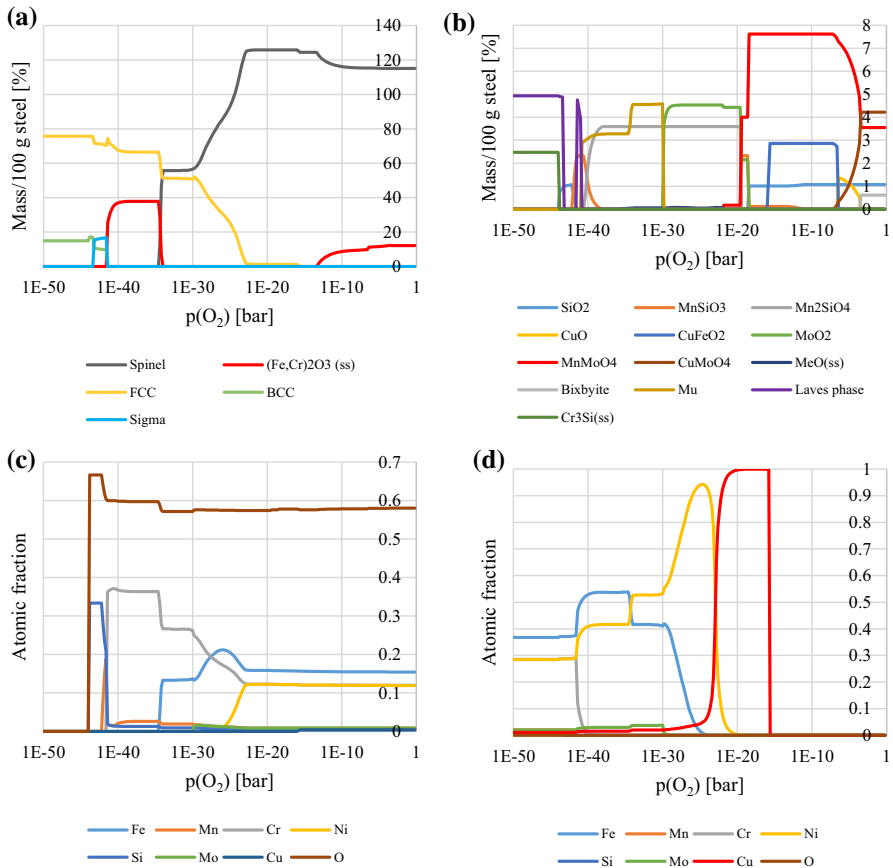

Fig. 14 Predicted phase equilibrium of the Sanicro 28 alloy at 500 °C as a function of p(O$_2$): major phases (**a**), minor phases (**b**), and the elemental composition of the oxide (**c**) and alloy phases (**d**)
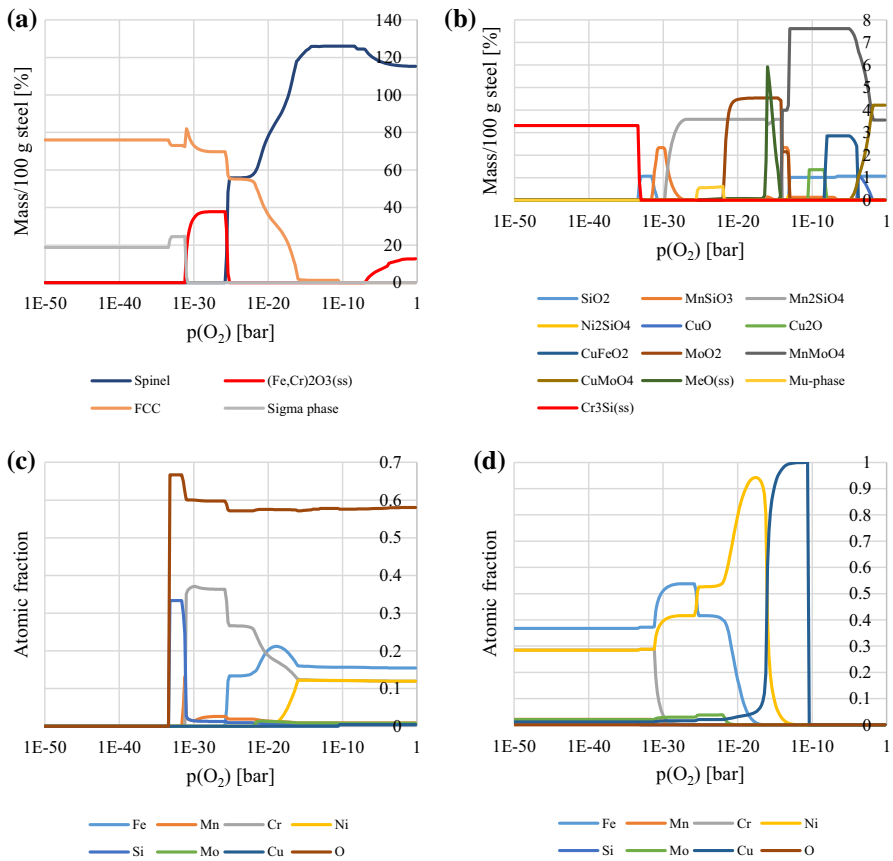
Fig. 15 Predicted phase equilibrium of the Sanicro 28 alloy at 700 °C as a function of p(O₂): major phases (**a**), minor phases (**b**), and the elemental composition of the oxide (**c**) and alloy phases (**d**)

mass transport mechanisms; from the outward transport of Fe cations and from the inward transport of O anions [17]. Although the oxide scale structure and oxidation behavior of low-alloyed Fe–Cr steels, in general, resembles those of pure iron, a few differences have been reported: the oxidation rate of a steel containing 2.25 wt% chromium is remarkably slower than that of pure iron and the alloyed chromium decreases the stability of the wüstite phase, thus preventing its formation above 570 °C, as takes place on pure iron [8, 18]. According to Eqs. 1 and 2 [19], the Gibbs free energy of formation, $\Delta_f G°$, is −615.7 and −566.0 kJ mol⁻¹ for hematite and −856.3 and −795.6 kJ mol⁻¹ for magnetite at 500 and 700 °C, respectively.

$$\Delta_f G°(\text{Fe}_2\text{O}_3)/\text{J mol}^{-1} = -818{,}930 + 348.39\ (\text{T/K}) - 12.866\ (\text{T/K})\ \ln(\text{T/K})$$

(1)

$$\Delta_f G°(\text{Fe}_3\text{O}_4)/\text{J mol}^{-1} = -1{,}094{,}200 + 331.67(\text{T/K}) - 3.6056(\text{T/K}) \ln(\text{T/K})$$

(2)

In the temperature region below 750 °C, the oxidation kinetics of a low-alloyed steel follows initially a parabolic rate law for the first couple of hours, after what a linear rate law is valid [20]. Since chromium is internally oxidized, the network of line-like structures at the sample surfaces at 200 °C (Fig. 2b) is most likely Fe_3O_4 nuclei, forming along the grain boundaries. These grain boundaries are suitable pathways for faster diffusion in low-alloyed Fe–Cr steels. Compared to the point defect-related lattice diffusion, grain boundary diffusion is considered to be important at low temperatures due to the lower activation energy for grain boundary diffusion and smaller grain size [16]. Factors such as the presence of defective substrate sites, the orientation, and perfection of the substrate facilitate cation vacancy diffusion through the thin oxide layer, resulting in Fe_3O_4 nuclei formation along the grain boundaries [21]. These nuclei form a porous, yet homogeneous oxide layer, over which Fe_2O_3 nuclei spread, first forming whiskers and then platelets at higher temperatures [22]. Typical whiskers and platelets can be seen for example in Fig. 3f, g.

The thickness of Fe_2O_3 formed on pure iron kept in a desiccator at room temperature has been measured to be around 3 nm [13, 23]. When measuring the oxide scale thickness using XPS in this work, the sputter voltage used was kept constant for all samples. This sputter rate was too fast for accurate thickness calculations in the case of very thin oxide layers. Therefore, the value (16.2 nm) presented in Table 1 differs greatly from the values reported earlier. Excluding the oxide scale thickness of the reference sample, the oxide scale thickens with increasing exposure temperature and time. The introduction of water into the furnace atmosphere increased the oxidation rate, resulting in thicker oxide scales compared to the dry conditions. These results are in line with the previously reported mass gains under humid conditions [18]. Although different iron oxide phases were not identified, based on the literature and on the thermodynamic predictions, the formed oxide scales consisted most likely of Fe_2O_3 and Fe_3O_4. The sample oxidized at 700 °C lacked the wüstite phase due to the solubility of chromium in the formed magnetite [21]. Some cavities also formed within the oxide scale. These cavities suggest the formation of a duplex iron oxide scale since pure iron cavities are located in the magnetite layer below the denser hematite layer [24].

Nb-Stabilized Austenitic AISI347 Steel

Although oxidation of pure niobium has been studied, only a few studies have been conducted with steels alloyed with niobium [25]. The oxidation of niobium initiates with a pre-transition period, during which a protective oxide scale containing various niobium oxides forms [16]. After the pre-transition period, first nuclei of Nb_2O_5 grow on the steel surface, where breakaway oxidation occurs resulting in local failures of the surface through the rapid formation of Nb_2O_5 [26]. The Gibbs free energy for formation of Nb_2O_5 at 800 K is -1545 kJ mol^{-1} [27]. The

stable Nb-concentration in the depth profiles indicates that the observed Nb-rich structures have formed as a result of Nb-oxidation in the vicinity of the surface rather than through Nb-diffusion from the bulk material toward the surface. In addition, no increase in Nb-concentration was observed in the elemental analyses, supporting the idea of local failure instead of homogeneous oxidation of niobium. Depending on the source, the Gibbs free energy for formation of Cr_2O_3 is reported to be -222 kJ mol^{-1} [28] or -921 kJ mol^{-1} [29] at 800 K and -209 kJ mol^{-1} [28] or -870 kJ mol^{-1} [29] at 1000 K. Despite the obvious discrepancy in the reported values, they differ clearly from the value for Nb_2O_5, supporting the observation of rapidly formed Nb_2O_5 particles. Although calculated for a higher temperature (1400 K), the Gibbs free energy for formation of the $FeCr_2O_4$ spinel is -214 kJmol^{-1} [30], further supporting the finding of Nb_2O_5 forming as the first oxide. The early oxidation of Nb was also predicted by the thermodynamic calculations. In Nb-stabilized austenitic stainless steel, NbC precipitates at the grain boundaries gave niobium oxide-enriched clusters at the scale surface during high-temperature oxidation [25]. These clusters were speculated to induce cracks and cavities in the oxide scale, thus enhancing formation of breakaway nodules.

The thickness of the oxide scale grown on ferritic and austenitic stainless steels at room temperature is typically 0.5–4 nm. The layer consists mainly of chromium species $Cr(OH)_3$ and Fe–Cr oxides, presumably $(Fe,Cr)_2O_3$ and $FeCr_2O_4$ [31]. Excluding the difficulty in using XPS to measure oxide scale thickness of the reference sample, i.e., layer thickness at room temperature, the oxide scale thickness of the other samples studied increased as functions of time and temperature. Thicker scales were measured at the ferritic steel. If the thicknesses of the oxide scales formed during the two exposure times are compared, their ratios are very close to one another at 200 °C (1.18) and at 500 °C (1.08), indicating that the oxidation rate remained the same at these temperatures for the 24-h exposure. At 700 °C, the thickness of the oxide scale formed in 24 h is almost sevenfold compared to the thickness of the oxide formed in 5 h, indicating accelerated oxide growth at this temperature. The presence of water did not affect the oxide scale thickness, which remained unaltered at 500 °C also during longer exposure times [32]. Under humid conditions, however, loss of protective properties of the oxide scale may occur through chromium volatilization as $CrO_2(OH)_2$. On the other hand, chromia volatilization has been reported to take place at slightly higher temperatures, 600 °C [33].

The different phases in the oxide scale with the outermost iron-rich layer followed by a chromium-rich inner layer could not be identified from the XPS data. The oxide scale was most likely a mixture consisting of corundum-structured phases of Fe_2O_3, $Fe_{2-x}Cr_xO_3$, and Cr_2O_3 [34]. The Ni-enriched region detected below the oxide scales in some depth profiles was assumed to originate from the depletion of iron and/or chromium through outward diffusion rather than from the diffusion of nickel from the bulk material to the interface below the oxide scale. Although the oxide scale composition was the same at 500 °C under dry and humid conditions, the relative amount of chromium compared to iron was higher under the humid conditions. The presence of water vapor is known to increase the amount of cation vacancies, leading to accelerated chromium diffusion [35]. However, the prevailing

conditions were mild enough to prevent breakaway oxidation. The breakaway oxidation is recognized to originate from chromium evaporation, resulting in chromium depletion in the oxide scale and eventually also in the loss of protective properties of the scale. The measured decrease in the chromium content just below the oxide scale is not an artifact, but it was assumed to evidence the chromium diffusion along the grain boundaries of the bulk material near the steel/oxide scale interface into the thickening oxide scale. Interestingly, no Cr-depleted region could be identified in the samples oxidized at 700 °C. This might originate from enhanced chromium supply from the bulk material due to the increased temperature, which has relocated the Cr-depleted region deeper in the bulk material beyond the analysis depth. The Mn-enrichment in the outermost layer of the oxide scale formed in 5 h at 700 °C indicates the presence of $Mn_{1.5}Cr_{1.5}O_4$ spinel [10]. Fast diffusivity of manganese through chromia has been reported to form a Mn-rich outer layer of the oxide surface [36]. At the longer exposures, the primarily formed Mn-rich surface layer was assumed to be covered by a thick chromia layer. Similar order of oxidation (manganese is oxidized prior to chromium) was also predicted by the thermodynamic calculations.

The loss of protective properties of the Fe–Cr alloys manifests in the rapid outward growth of iron oxide, also known as breakaway oxidation. Hence, it is worth mentioning that although the continuous oxide scale formed on the AISI 347 steel samples was damaged by the locally formed Nb_2O_5 nodules, it still consisted of Fe–Cr oxide (500 °C) or chromium oxide (700 °C), indicating that oxidation of the steel had not yet entered the breakaway state. However, it should be borne in mind that various aggressive gaseous species such as HCl and chlorides present in the boiler environment may change the corrosion mechanism and rate by penetrating the otherwise protective oxide scale through the above-mentioned local failures.

High Alloy Austenitic Sanicro 28 Steel

The 4- to 11-nm passive oxide layer on high Fe–Cr–Ni ferritic and austenitic stainless alloys at room temperature consists mainly of chromium species $Cr(OH)_3$ and Cr_2O_3 [15]. At elevated temperatures (600 °C) and under dry conditions the protective oxide scale formed on these alloys consists of a duplex Fe–Cr structure with an iron-rich outermost layer and chromium-rich inner layer with no nickel [37]. The Gibbs free energy for formation of NiO at 500 and at 700 °C is −168 and −151 kJ mol^{-1}, respectively [38]. In Ni–Cr alloys, NiO and Cr_2O_3 can form a spinel-structured $NiCr_2O_4$. The Gibbs free energy of formation of $NiCr_2O_4$ is −149 kJ mol^{-1} at 800 K and of −211 kJ mol^{-1} at 1000 K [39]. Although the Gibbs free energy values for NiO and $NiCr_2O_4$ are close to one another, the absence of Ni-containing oxides can be explained by the high Cr-content of the Sanicro 28 steel (25.9 wt%). In Ni–Cr steels, the selective oxidation of chromium occurs when the Cr-content is above roughly 20 wt% [16]. The absence of a Ni-containing oxide was also predicted with the thermodynamic calculations, according to which Cr and Mn oxidize first, followed by the oxidation of Fe.

The high alloy austenitic Sanicro 28 steel samples under dry conditions at 200 and 500 °C formed similar scale structure consisting of an iron-rich outer layer and a chromium-rich inner layer. At 500 °C, the presence of water vapor did not alter significantly the chemical composition of the protective oxide scale at the Sanicro 28 steel. According to X-ray diffraction (XRD), the scale consists of corundum type α-$(FeCr)_2O_3$ and spinel type (M_3O_4) oxides [40]. However, in this work, the detected chromium-depleted area underneath the oxide scale suggests that the presence of water vapor accelerated chromium diffusion from the bulk material to the surface. As discussed above, chromium evaporation as chromium(VI)oxyhydroxide may partly explain the observed chromium depletion, which has been reported (e.g., 41) to form at least at a slightly higher temperature (600 °C) (Eq. 3). Another explanation for the increased chromium diffusion could be the increased cation vacancy concentration in the oxide scale, which compensates the increased concentration of hydroxyl defects caused by water vapor [35]. Since the oxide scale thickness is virtually the same under dry and humid conditions at 500 °C, the presence of water vapor appears to only have influenced chromium diffusivity, not the oxide scale growth rate. The detected Ni- and Mn-enrichments underneath the oxide scale might originate from the bigger relative concentrations of these elements due to the Cr-depletion.

$$2Cr_2O_3(s) + 3O_2(g) + 4H_2O(g) \rightarrow 4CrO_2(OH)_2(g) \qquad (3)$$
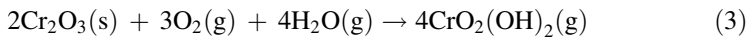
The almost pure chromia scale formed at 700 °C during both exposure times suggests that although the oxide scales have grown thicker, they have maintained the protective properties instead of entering the breakaway stage of oxidation. If the thicknesses of the oxide scales formed during the two exposure times are compared with one another, the ratios between the oxide formed during 24 h and the oxide formed during 5 h grew only slightly as a function of temperature, being 1.19 at 200, 1.43 at 500 and 1.50 at 700 °C. This suggests smaller influence of time on oxidation rate of the high alloy austenitic Sanicro 28 steel samples during the first 24 h as compared to the oxidation rate of the Nb-stabilized austenitic AISI347 steel. This can be attributed to the different chromium contents of the two steels, AISI 347 with 17.7 wt% and Sanicro 25.9 wt%. Although selective oxidation of chromium is more easily established on Fe–Cr steels than on Ni–Cr steels due to greater interdiffusion and smaller oxygen solubility and diffusivity in Fe–Cr steels [16], it requires the excess of a certain threshold value for chromium concentration. This threshold value is reported to be roughly 20 wt% [6]. The chromium content in the AISI 347 steel stays below the threshold concentration, precluding the selective formation of the chromium oxide scale, whereas the chromium content in the Sanicro 28 steel enables the formation of the protective scale.

Conclusions

The effect of pre-oxidation conditions on the oxide scale composition, thickness, and morphology three commercial steels: a low alloy ferritic 10CrMo9-10 steel, a Nb-stabilized austenitic AISI347 steel, and a high alloy austenitic Sanicro 28 steel were studied.

In the low alloy ferritic 10CrMo9-10 steel, the oxide scale thickness increased as functions of temperature and time. Despite the pre-oxidation conditions, the oxide scale consisted of iron oxide, which appeared to initially form along the surface grain boundaries at 200 °C, then covered the surface more homogeneously with a structure consisting of Fe_2O_3 whiskers at 500 °C and finally formed a thick, porous iron oxide over the whole surface at 700 °C.

A duplex oxide scale with an iron-rich outer and a chromium-rich inner layer formed on the Nb-stabilized austenitic AISI347 steel at 200 and 500 °C. Interestingly, niobium oxide nodules formed at 500 °C in an uncontrolled manner. These nodules were assumed to provide a diffusion pathway for corrosive species typically present in biomass-combusting environments to penetrate through the oxide scale to the unprotected steel surface. At 700 °C, the oxide scale consisted of almost pure chromium oxide. However, the surface morphology of the chromium oxide scale suggests that the scale does not protect the steel in the presence of corrosive species such as KCl or HCl.

Thinnest oxide scales formed on the high alloy austenitic Sanicro 28 steel under all test conditions. The oxide scale had a duplex structure with an iron-rich outer layer and a chromium-rich inner layer at 200 or at 500 °C. An almost pure chromium oxide scale formed at 700 °C, but unlike on the Nb-stabilized austenitic AISI347 steel, scale on the high alloy austenitic Sanicro 28 steel had smaller grain size variation and appeared to the non-porous and well adhered to the surface.

The presence of water affected only the oxide scale thickness of the low alloy ferritic 10CrMo9-10 steel, while on the other two steels, accelerated chromium diffusion from the bulk material to the oxide scale took place without increasing the oxide growth rate.

References

1. M. Spiegel, *Materials and Corrosion* **50**(7) 373 (1999).
2. L. A. Hansen, H. P. Nielsen, F. J. Frandsen, K. Dam-Johansen, S. Hørlyck and A. Karlsson, *Fuel Processing Technology* **64**(1–3) 189 (2000).
3. L. Åmand, B. Leckner, D. Eskilsson and C. Tullin, *Energy & Fuels* **20**(3) 1001 (2006).

4. H. P. Nielsen, F. J. Frandsen, K. Dam-Johansen and L. L. Baxter, *Progress in Energy and Combustion Science* **26**(3) 283 (2000).
5. D. Bankiewicz, *Corrosion behavior of boiler tube materials during combustion of fuels containing Zn and Pb*, (Academic Dissertation, Åbo Akademi University, Department of Chemical Engineering, Turku, Finland, 2012).
6. N. Birks, G. H. Meier and F. S. Pettit, *Introduction to the High-Temperature Oxidation of Metals*, 2nd ed, (Cambridge University Press, Cambridge, 2006).
7. J. Stringer, *Materials Science & Engineering, A: Structural Materials: Properties, Microstructure and Processing* **A120–A121** 129 (1989).
8. A. S. Khanna, *Introduction to High Temperature Oxidation and Corrosion*, (ASM International, Ohio, 2002).
9. N. Israelsson, J. Engkvist, K. Hellstroem, M. Halvarsson, J.-E. Svensson and L.-G. Johansson, *Oxidation of Metals* **83**(1–2) 29 (2015).
10. H. Buscail, S. El Messki, F. Riffard, S. Perrier and C. Issartel, *Oxidation of Metals* **75**(1–2) 27 (2011).
11. C. W. Bale, E. Bélisle, P. Chartrand, S. A. Decterov, G. Eriksson, A. E. Gheribi, K. Hack, I.-H. Jung, Y.-B. Kang, J. Melançon, A. D. Pelton, S. Petersen, C. Robelin, J. Sangster, P. Spencer and M.-A. Van Ende, *Calphad* **54** 35 (2016).
12. D. R. Baer, M. H. Engelhard, A. S. Lea, P. Nachimuthu, T. C. Droubay, J. Kim, B. Lee, C. Mathews, R. L. Opila, L. V. Saraf, W. F. Stickle, R. M. Wallace and B. S. Wright, *Journal of Vacuum Science & Technology A* **28**(5) 1060 (2010).
13. H. J. Mathieu, M. Datta and D. Landolt, *Journal of Vacuum Science & Technology A* **3**(2) 331 (1985).
14. C.-O. A. Olsson, S. Malmgren, M. Gorgoi and K. Edström, *Electrochemical and Solid-State Letters* **14**(1) C1 (2011).
15. G. Lothongkum, S. Chaikittisilp and A. W. Lothongkum, *Applied Surface Science* **218** 202 (2003).
16. P. Kofstad, *High Temperature Corrosion*, (Elsevier Applied Science Publishers Ltd., London and New York, 1988).
17. V. B. Trindade, U. Krupp, Ph E-G Wagenhuber and H.-J. Christ, *Materials and Corrosion* **56**(11) 785 (2005).
18. B. Pujilaksono, T. Jonsson, H. Heidari, M. Halvarsson, J.-E. Svensson and L.-G. Johansson, *Oxidation of Metals* **75**(3–4) 183 (2011).
19. E. Jacobsson, *Scandinavian Journal of Metallurgy* **14** 252 (1985).
20. A. Skalli, A. Galerie and M. Caillet, *Solid State Ionics* **25**(1) 27 (1987).
21. B. Chattopadhyay and G. C. Wood, *Oxidation of Metals* **2**(4) 373 1970.
22. U. R. Evans, *The Corrosion and Oxidation of Metals: First Supplementary Volume*, (Edward Arnold Publishers Ltd., London, 1968).
23. R. L. Tapping, R. D. Davidson, T. E. Jackman and J. A. Davies, *Surface and Interface Analysis* **11**(8) 441 (1988).
24. B. Pujilaksono, T. Jonsson, M. Halvarsson, J.-E. Svensson and L.-G. Johansson, *Corrosion Science* **52** (5) 1560 (2010).
25. H. Viitala, I. Galfi and P. Taskinen, *Materials and Corrosion* **66**(9) 851 (2015).
26. J. V. Cathcart, J. J. Campbell and G. P. Smith, *Journal of the Electrochemical Society* **105**(8) 442 (1958).
27. K. T. Jacob, C. Shekhar and M. Vinay, *Journal of Chemical Engineering & Data* **55**(11) 4854 (2010).
28. J. P. Coughlin, *U.S. Bureau of Mines Bulletin* **542** 68 (1954).
29. A. Mittal, G. J. Albertsson, G. S. Gupta, S. Seetharaman and S. Subramanian, *Metallurgical and Materials Transactions B* **45B** 338 (2014).
30. S. E. Ziemniak, L. M. Anovitz, R. A. Castelli and W. D. Porter, *The Journal of Chemical Thermodynamics* **39**(11) 1474 (2007).
31. S. Jin and A. Atrens, *Applied Physics A* **A50**(3) 287 (1990).
32. J. Lehmusto, B.-J. Skrifvars, P. Yrjas and M. Hupa, *Fuel Processing Technology* **105** 98 (2013).
33. M. Halvarsson, J. E. Tang, H. Asteman, J.-E. Svensson and L.-G. Johansson, *Corrosion Science* **48**(8) 2014 (2006).
34. A. Srisrual, J.-P. Petit, Y. Wouters and A. Galerie, *Oxidation of Metals* **79**(3–4) 337 (2013).
35. S. R. J. Saunders, M. Monteiro and F. Rizzo, *Progress in Materials Science* **53**(5) 775 (2008).
36. C. Ostwald and H. J. Grabke, *Corrosion Science* **46**(5) 1113 (2004).
37. L. Intiso, L.-G. Johansson, S. Canovic, S. Bellini, J.-E. Svensson and M. Halvarsson, *Oxidation of Metals* **77**(5–6) 209 (2012).
38. H. Comert and J. N. Pratt, *The Journal of Chemical Thermodynamics* **16**12 1145 (1984).

39. E. B. Rudnyi, E. A. Kaibicheva, L. N. Sidorov, M. T. Varshavskii and A. N. Men, *The Journal of Chemical Thermodynamics* **22**(7) 623 (1990).
40. C. Proff, T. Jonsson, C. Pettersson, J.-E. Svensson, L.-G. Johansson and M. Halvarsson, *Materials at High Temperatures* **26**(2) 113 (2009).
41. C. Pettersson, L.-G. Johansson and J.-E. Svensson, *Oxidation of Metals* **70**(5–6) 241 (2008).